

A MEMS stage for 3-axis nanopositioning

Xinyu Liu, Keekyoung Kim and Yu Sun

Department of Mechanical and Industrial Engineering, University of Toronto,
5 King's College Road, Toronto, ON M5S 3G8, Canada

E-mail: sun@mie.utoronto.ca

Received 2 May 2007, in final form 10 July 2007

Published 3 August 2007

Online at stacks.iop.org/JMM/17/1796

Abstract

Applications in micro- and nanotechnologies require millimeter-sized devices that are capable of 3-axis positioning with motion ranges of micrometers and resolutions of nanometers. This paper reports on the design, fabrication and testing of a MEMS-based 3-axis positioning stage. In-plane (comb-drive) and out-of-plane (parallel-plate) electrostatic actuators are employed for driving the stage to move independently along the XYZ directions, by $\pm 12.5 \mu\text{m}$ in the X and Y directions at an actuation voltage of 30 V and by $3.5 \mu\text{m}$ in the Z direction at 14.8 V. The structures are designed to achieve highly decoupled motions by effectively suppressing cross-axis motion coupling. The open-loop positioning repeatability is determined to be better than 17.3 nm along all three axes.

(Some figures in this article are in colour only in the electronic version)

1. Introduction

A variety of applications in micro- and nanotechnologies, such as optical cross connect (OXC) [1], micro confocal imaging [2] and scanning probe microscopy (SPM) based high-density data storage [3], demand the capability of positioning over a motion range of micrometers and with a resolution of nanometers, ideally along three independent axes. Consequently, the development of nanopositioning stages has rapidly evolved during the past decade.

Piezoelectric electron-discharge-machined stages have been widely used for nanopositioning applications [4, 5]. Although piezoelectric stages are capable of providing nanometer positioning resolutions, inherent hysteresis and creep of piezoelectric actuators can cause significant open-loop positioning errors, and thus, require nonlinear compensation [6, 7]. Besides the high cost, the large sizes of most commercially available piezoelectric stages (e.g., 10 cm) limit their use when applications have stringent space restrictions [3, 8].

MEMS (microelectromechanical systems) based positioning stages are appealing due to their low cost, small size, fast response and flexibility for system integration. Furthermore, microfabrication permits arrays of MEMS positioning stages to be readily constructed on a common substrate for achieving highly efficient parallel manipulation tasks, such as parallel SPM imaging [9] and microlens-array-based OXC [10, 11].

Several MEMS positioning stages, using different mechanical structures and actuation principles, have been reported [2, 3, 12–25]. There is a vast literature on devices producing only out-of-plane torsional motions for micromirror applications (e.g., [12–16]). Differently, this paper focuses on MEMS stages for producing translational motions [2, 3, 17–25]. Most existing positioning stages are capable of generating only in-plane translational motions [2, 3, 17–22], while attempts to construct devices producing both in-plane (XY) and out-of-plane (Z) translational motions are fewer [23–25].

A surface-micromachined XYZ stage was developed for optical scanning and alignment [23]. Without vertical actuators, the device uses scratch drive actuators to generate in-plane translational motions that are converted into vertical motions by hinges. In order to simultaneously produce in-plane translational motions and out-of-plane displacements, the multiple in-plane scratch drive actuators must be carefully, coordinately controlled. In addition, completely decoupling horizontal and vertical motions is difficult due to the lack of a dedicated vertical actuator.

A recently reported 3-axis electrostatic stage [24] employed leaf springs inclined to the substrate to transform in-plane displacements into out-of-plane displacements. The drawback of this design is that the horizontal and vertical motions are coupled by the inclined springs, making it impossible to control XYZ motions independently. The motion range of the design is also limited ($\leq 1.1 \mu\text{m}$ in XYZ

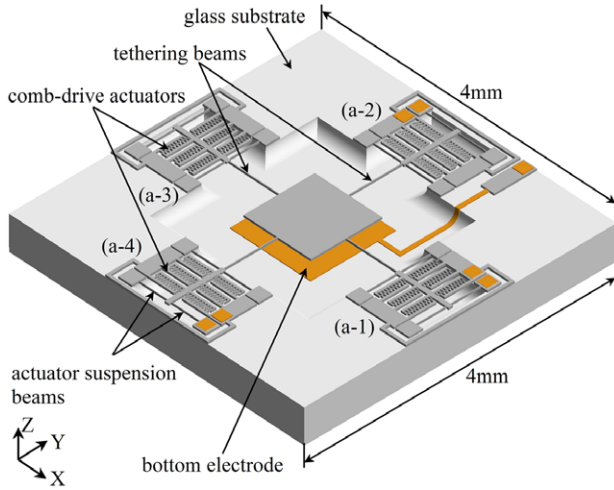


Figure 1. Solid model of the bulked micromachined 3-axis MEMS positioning stage.

directions at 100 V).

Instead of transforming horizontal motions into vertical motions, integrating dedicated vertical actuators is more effective for achieving independent out-of-plane displacements. More recently, a bulk micromachined XYZ stage integrating in-plane comb-drive actuators and a vertical comb-drive actuator was reported [25]. Although the device is capable of generating decoupled XYZ motions, the vertical comb drive actuator requires a very high actuation voltage for producing small vertical displacements ($2 \mu\text{m}$ at 240 V).

This paper presents the design, fabrication and testing of a 3-axis electrostatic positioning stage that produces highly decoupled XYZ motions of micrometers at low actuation voltages (up to 30 V). Comb-drive actuators are used to move the center stage in the X and Y directions, and a parallel-plate electrostatic actuator positions the center stage vertically. The mechanical structures are designed to minimize coupling among different axes. A silicon-on-glass process is employed to construct the 3-axis MEMS positioning stages.

2. Working principle

Figure 1 shows a schematic diagram of the 3-axis positioning stage. The in-plane structures are fabricated on a silicon layer on top of a patterned glass substrate. On the silicon layer, four comb-drive actuators are distributed around the center stage ($1000 \times 1000 \mu\text{m}$), driving the center stage along the X and Y directions. Four tethering beams are used for suspending the center stage and transmitting in-plane motions from the comb-drive actuators. The center stage and a bottom metal electrode on the recessed glass substrate form a parallel-plate actuator to drive the center stage vertically. The bottom electrode has a slightly larger area than the center stage to keep the overlapping area constant during in-plane actuation.

The orthogonal configuration of the XYZ actuators permits the minimization of motion coupling among different directions. As an example, when the in-plane actuator (a-1) drives the center stage along the X direction, both tethering beams along the X direction are in a tensile state, and no displacements along the Y direction are produced. The

actuation force along the X direction deflects the two tethering beams in the Y direction and also applies X -directional loads to the suspension beams of actuators (a-2) and (a-4). As it is desired to minimize X -directional displacements of the movable comb fingers of (a-2) and (a-4) in order not to interfere with simultaneous positioning of the center stage along the Y direction, the suspension beams of (a-2) and (a-4) must have a high lateral stiffness along the X direction. In this design, four fixed-guided suspension beams (figure 1) are used for each comb-drive actuator, providing a high lateral stiffness of $2.99 \times 10^4 \mu\text{N} \mu\text{m}^{-1}$.

When the center stage is actuated in the Z direction, both tethering beams and actuator suspension beams are deflected vertically. The vertical stiffness of the actuator suspension beams is set to be 13 times higher than that of the tethering beams in order to suppress the vertical deflection of comb fingers, and thus, cause little change of in-plane actuation forces to achieve decoupled, simultaneous positioning along all three axes.

3. Theoretical analysis

3.1. In-plane analysis

In-plane and out-of-plane stiffness of the 3-axis positioner is analyzed, and the relationships between actuation voltages and resulting displacements in the XYZ directions are established to provide a systematic design approach for determining device parameters. In the analysis, it is assumed that the stiffness in one direction is not significantly affected by the structural deformations along other directions. The assumption is justified under small deformation conditions that hold in this design. Finite element simulation also confirms that the design operates in the linear region throughout the working span.

Ignoring the high lateral stiffness of actuator suspension beams, the in-plane stiffness of the device is [26]

$$K_{x,y} = \frac{8Ehw^3}{l^3} + \frac{2EHW^3}{L^3} \quad (1)$$

where E is Young's modulus of silicon, w , h and l are the width, height and length of actuator suspension beams, and W , H and L are the width, height and length of tethering beams.

The electrostatic force generated by a comb-drive actuator is

$$F = \frac{1}{2} \frac{N_a \epsilon h_a}{g_a} V_{x,y}^2 \quad (2)$$

where $\epsilon = 8.85 \times 10^{-12} \text{C}^2 \text{N}^{-1} \text{m}^{-2}$ is the permittivity of air, N_a the number of actuation comb finger pairs, h_a the finger thickness, g_a the gap between adjacent comb fingers and $V_{x,y}$ the in-plane actuation voltage. Thus, in-plane displacements are

$$x, y = \pm \frac{F}{K_{x,y}} = \pm \frac{N_a \epsilon h_a}{2g_a K_{x,y}} V_{x,y}^2 \quad (3)$$

where the plus/minus signs represent backward and forward motions.

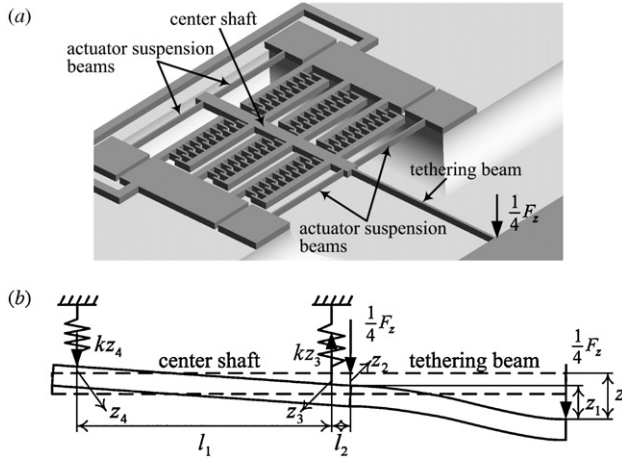


Figure 2. Vertical stiffness analysis. (a) Structural detail of one group of tethering and suspension beams. (b) Analytical model.

3.2. Out-of-plane analysis

The vertical stiffness of the suspended structure is determined via a static force analysis of the tethering and suspension beams. Due to symmetry, only one group of tethering and suspension beams with equivalent boundary conditions is considered, as illustrated in figure 2.

The vertical electrostatic force, F_z , applied to the center stage results in deflections of the tethering and suspension beams. The equivalent force in the analytical model, shown in figure 2(b), is a quarter of F_z . The deflection of the tethering beam is denoted by z_1 , and the vertical displacement of the connecting interface between the tethering beam and the center shaft is denoted by z_2 . Due to the high stiffness of the center shaft, it is regarded as a rigid body, which is tilted with a small angle. The two sets of suspension beams at each end of the center shaft are considered as linear springs with small deflections. The elongation/compression displacements of the two sets of linear springs are denoted by z_3 and z_4 . The total vertical displacement of the center stage is z .

Force balancing of the deflected tethering beam gives

$$\frac{1}{4}F_z = Kz_1 \quad (4)$$

where $K = EWH^3/L^3$ is the vertical stiffness of the tethering beam.

A static analysis of the tilted center shaft yields the following force and torque equilibrium equations:

$$\frac{1}{4}F_z l_2 = kz_4 l_1 \quad (5)$$

$$\frac{1}{4}F_z + kz_4 = kz_3 \quad (6)$$

where $k = 2Ewh^3/l^3$ is the spring constant of two fixed-guided suspension beams.

Additionally, trigonometry gives

$$\frac{l_1}{l_2} = \frac{z_3 + z_4}{z_2 - z_3} \quad (7)$$

Solving equations (4), (5), (6) and (7) yields

$$z_1 = \frac{F_z L^3}{4EWH^3} \quad (8)$$

Table 1. Design parameters of the 3-axis stage.

Mechanical properties of silicon	
Young's modulus	129.5 Gpa
Poisson's ratio	0.28
Structural parameters	
Tethering beams	$W = 4 \mu\text{m}, H = 10 \mu\text{m}, L = 750 \mu\text{m}$
Suspension beams	$w = 2.5 \mu\text{m}, h = 10 \mu\text{m}, l = 420 \mu\text{m}$
Center stage	$1.0 \text{ mm} \times 1.0 \text{ mm}$
Center shaft	$l_1 = 578.5 \mu\text{m}, l_2 = 21.25 \mu\text{m}$
Actuation parameters	
Comb-drive actuator	$N_a = 1592, h_a = 10 \mu\text{m}, g_a = 2 \mu\text{m}$
Parallel-plate actuator	$A = 1.0 \text{ mm}^2, d = 12 \mu\text{m}$

$$z_2 = \frac{F_z l^3 \alpha}{8Ewh^3} \quad (9)$$

where α is a constant determined by the structural parameters of the center shaft:

$$\alpha = 1 + 2\frac{l_2}{l_1} + 2\left(\frac{l_2}{l_1}\right)^2 \quad (10)$$

Thus, the total vertical stiffness of the device is

$$K_z = \frac{F_z}{z} = \frac{F_z}{z_1 + z_2} = \frac{4Kk}{K\alpha + k} \quad (11)$$

The parallel-plate actuator generates electrostatic forces

$$F_z = \frac{1}{2} \frac{\epsilon A}{(d - z)^2} V_z^2 \quad (12)$$

where A is the overlapping area of the parallel plates, d the initial gap and V_z the vertical actuation voltage. When the center stage reaches equilibrium, the electrostatic force is balanced by mechanical restoring forces. The resulting vertical displacement is

$$z = \frac{1}{2} \frac{\epsilon A}{K_z (d - z)^2} V_z^2 \quad (13)$$

Based on (3) and (13), the design parameters of the 3-axis positioner are determined and summarized in table 1.

4. Microfabrication

The 3-axis MEMS positioning stages were constructed using a silicon on glass substrate process. A glass wafer and a silicon-on-insulator (SOI) wafer were used and processed with wet glass etching, anodic bonding, wet silicon etching and silicon deep reactive ion etching (DRIE). The fabrication process, as illustrated in figure 3, is briefly described as follows.

- Step A.* Microfabrication starts with a $500 \mu\text{m}$ thick Pyrex wafer, on which $12 \mu\text{m}$ deep recesses are formed by BOE etching.
- Step B.* Metal electrode and connecting metal stripes, consisting of 500 \AA thick Ti-W and 2000 \AA Au are patterned on the etched and non-etched surfaces of the glass wafer using sputtering and lift-off.
- Step C.* An SOI wafer is anodically bonded to the patterned glass wafer with the device layer ($10 \mu\text{m}$ thick) facing down.

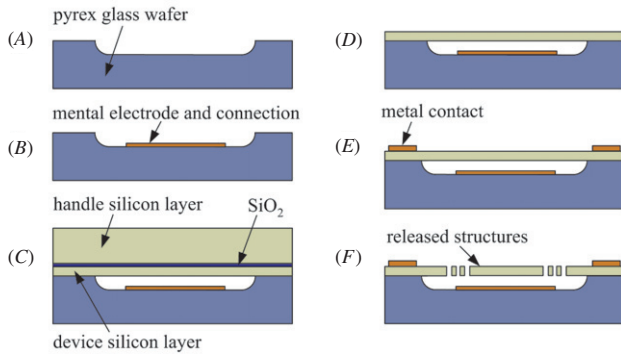


Figure 3. Microfabrication process for constructing 3-axis positioning stages.

Step D. The handle silicon layer and buried SiO₂ box layer are removed using wet etching (KOH for silicon and BOE for SiO₂), leaving only the single crystal silicon device layer on top of the glass substrate.

Step E. Metal layers of 500 Å thick Ti–W and 2000 Å Au are evaporated onto the device layer to form ohmic contacts, and are patterned using wet etching.

Step F. The device layer is finally etched through using DRIE to form comb fingers, center stage, tethering beams, actuation suspension beams and other features.

Figure 4 shows a released device with detailed views of the parallel-plate actuator and a comb-drive actuator.

5. Testing results

The device was glued and wire-bonded onto a ceramic package for testing. A dc power supply (AMREL SPS600-2) was used to provide actuation voltages of 0–30 V. The in-plane displacements of the stage were measured under an optical

Table 2. Measured post-fabrication dimensions.

Tethering beams	$W = 3.87 \mu\text{m}$, $H = 9.65 \mu\text{m}$, $L = 752.11 \mu\text{m}$
Suspension beams	$w = 2.39 \mu\text{m}$, $h = 9.65 \mu\text{m}$, $l = 421.50 \mu\text{m}$
Center stage	$998.71 \mu\text{m} \times 999.25 \mu\text{m}$
Center shaft	$l_1 = 577.23 \mu\text{m}$, $l_2 = 21.14 \mu\text{m}$
Comb-drive actuator	$h_a = 9.65 \mu\text{m}$, $g_a = 2.18 \mu\text{m}$
Parallel-plate actuator	$A = 0.998 \text{ mm}^2$, $d = 11.95 \mu\text{m}$

microscope (100 × objective, NA 0.42) with a digital camera (Nikon Coolpix 8400, 3.5 × optical lens, 3264 × 2488 pixels). The pixel size was calibrated to be 32.26 nm/pixel. The captured images were post-processed by tracking the movable features with a sub-pixel auto-correlation algorithm [27]. The tracking resolution was determined to be 0.08 pixel, and thus the measurement resolution of in-plane displacements is 2.58 nm with the testing setup. Vertical motions were measured by an optical interferometer (Wyko NT1100, Veeco) with a measurement resolution of 7.1 nm.

Figure 5 shows the testing results of in-plane displacements versus actuation voltage squared. At 30 V, the positioning stage produces $\pm 12.5 \mu\text{m}$ displacements along both X and Y directions. Figure 6 shows the testing results of vertical displacements versus actuation voltages. The parallel-plate actuator produces $3.5 \mu\text{m}$ vertical displacements with an actuation voltage of 14.8 V, beyond which pull-in occurs. As microfabrication can cause dimensional deviations, post-fabrication measurements were conducted and summarized in table 2. The measured dimensions were fitted into the theoretical models, (3) and (13). As shown in figures 5 and 6, theoretical predictions for both in-plane and out-of-plane positioning are in agreement with the testing results.

In order to quantify XYZ decoupling of the positioning stage, displacements in the un-actuated directions caused by

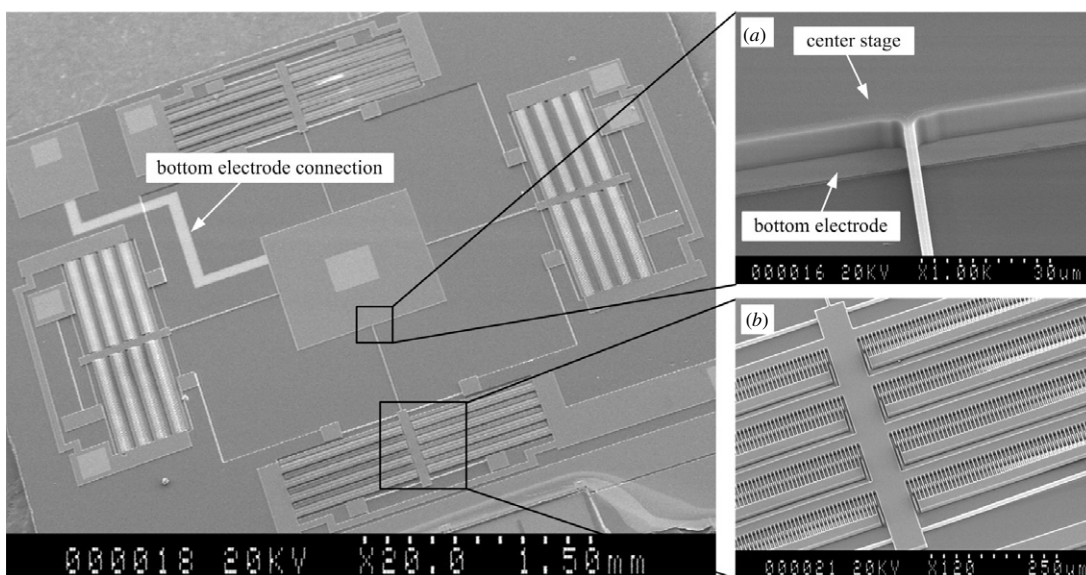


Figure 4. Scanning electron microscopy picture of a released device. The zoomed-in components are (a) the out-of-plane parallel-plate actuator and (b) the in-plane comb-drive actuator.

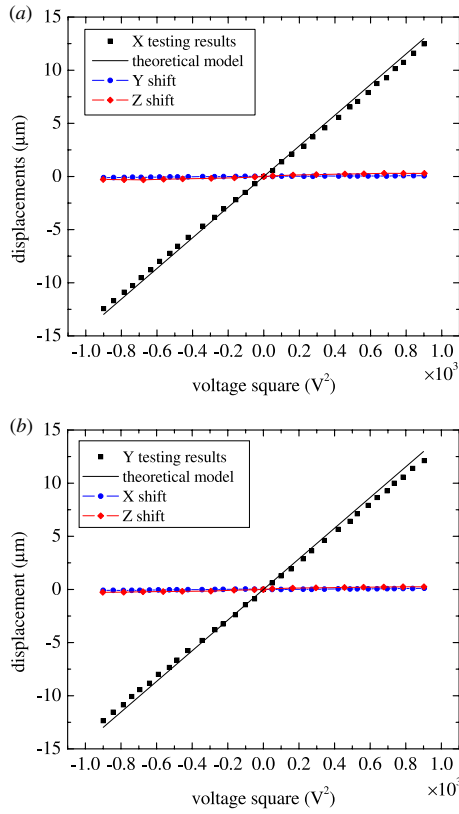


Figure 5. Testing results of in-plane displacements versus the actuation voltage squared. Also shown are coupling displacements along un-actuated directions. (a) Actuated along the X direction only. (b) Actuated along the Y direction only.

Table 3. Experimental results of the maximum coupled shifts in the XYZ directions.

Coupled shift (μm)	X	Y	Z
X	–	0.11	0.13
Y	0.11	–	0.16
Z	0.29	0.26	–

cross-axis coupling were also measured. The results are shown in figures 5 and 6. Table 3 summarizes the maximum coupled shifts in the XYZ directions, where dashes represent the actuated directions. For instance, when the stage is positioned along the X direction for $\pm 12.5 \mu\text{m}$, the maximum displacements in the Y and Z directions due to cross-axis coupling are $0.11 \mu\text{m}$ and $0.29 \mu\text{m}$, respectively. Due to the low vertical stiffness ($4.5 \mu\text{N} \mu\text{m}^{-1}$) of the stage, coupled shifts in the Z direction are always larger than the ones in the XY directions. Note that the reported cross-axis coupling results are coupled shifts on the center stage. Due to the high lateral stiffness of the actuator suspension beams, these coupled shifts on the center stage are significantly inhibited on the movable comb drives to be smaller than 0.05 nm that was determined in finite element simulation. The testing results demonstrate that the designed structure is effective in suppressing cross-axis coupling and achieving simultaneous, highly decoupled 3-axis positioning.

In addition, the positioning repeatability of the 3-axis stage was quantitated. The positioning stage was repeatedly

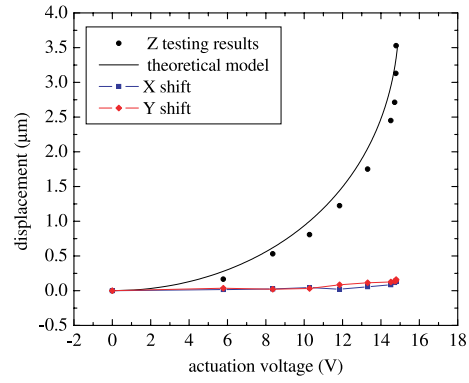


Figure 6. Testing results of vertical displacements versus actuation voltages. Also shown are coupling displacements along the XY directions.

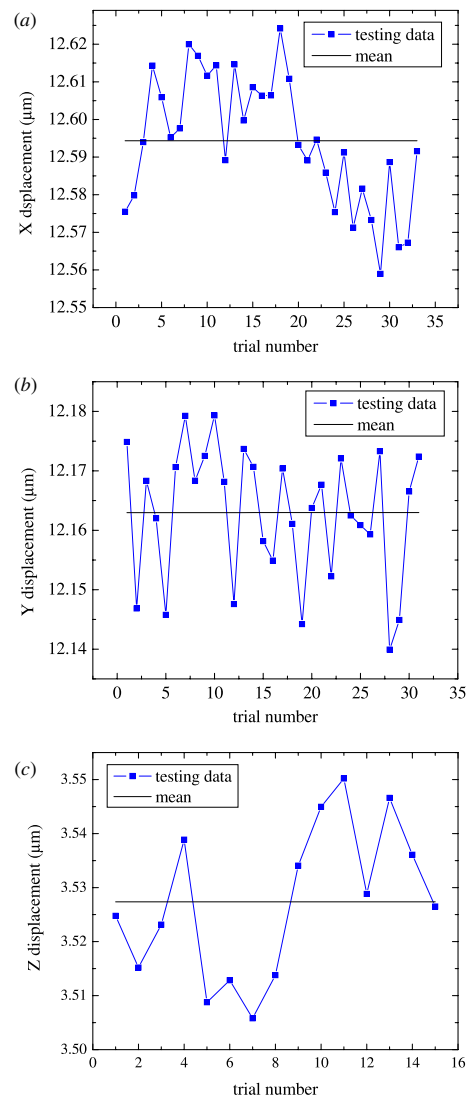


Figure 7. Testing results of positioning repeatability. (a) X direction. (b) Y direction. (c) Z direction.

actuated with the same actuation voltages (30 V in the XY directions and 14.8 V in the Z direction) to reach the maximum displacements in all XYZ directions. Figure 7 shows the

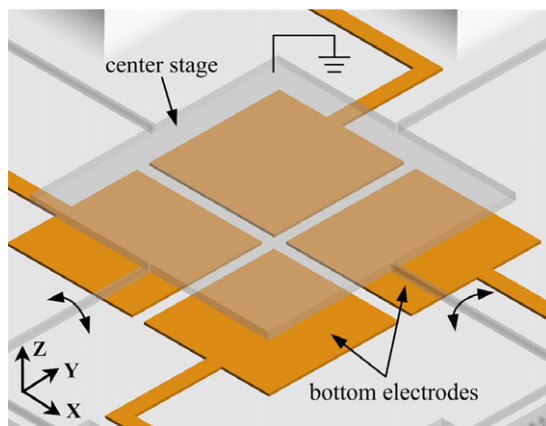


Figure 8. Schematic diagram of using separated bottom electrodes to generate both out-of-plane translational and torsional motions.

measured data in repeatability tests. The standard deviations of the maximum displacements were determined to be 17.3 nm, 11.1 nm and 14.2 nm in XYZ directions, demonstrating that the positioning stage has an open-loop repeatability better than 17.3 nm along all three axes.

6. Discussion

The positioning stage presented in this paper is capable of simultaneously producing $\pm 12.5 \mu\text{m}$ in-plane displacements at 30 V and $3.5 \mu\text{m}$ out-of-plane displacements at 14.8 V. The use of a parallel-plate actuator for vertical positioning makes the maximum vertical travel limited to approximately one-third of the total gap between the parallel plates. In order to overcome the pull-in limit and extend the stable travel range, closed-loop control [28, 29] can be conducted, which requires real-time acquisitions of position feedback. Alternatively, for open-loop positioning, the recess depth of the glass substrate can be increased to permit a larger vertical displacement, which certainly necessitates the application of larger vertical actuation voltages.

In the current design, the initial vertical deflection of the center stage, which is caused by gravity, was experimentally determined to be $\leq 0.06 \mu\text{m}$. When a $500 \mu\text{m} \times 500 \mu\text{m} \times 100 \mu\text{m}$ silicon sample was placed on top of the center stage for nanopositioning, the vertical deflection was measured to be $\leq 0.13 \mu\text{m}$. Additionally, driving the sample does not sacrifice the positioning performance of the stage.

The design presented in this paper has a single bottom electrode to form the out-of-plane parallel-plate actuator. By separating the bottom electrode into multiple regions (figure 8) and applying actuation voltages to selected electrodes, the MEMS stage will be able to produce both out-of-plane translational motions and out-of-plane torsional motions about the X and Y directions although tilting angles will be limited (smaller than 2°).

7. Conclusion

This paper presented a MEMS-based 3-axis positioning stage fabricated via a silicon-on-glass process. With both in-plane and out-of-plane actuators, the device is capable

of generating $\pm 12.5 \mu\text{m} \times \pm 12.5 \mu\text{m} \times 3.5 \mu\text{m}$ displacements, independently along the XYZ directions. The required actuation voltages are relatively low (30 V in the XY directions and 14.8 V in the Z direction). The stage structure provides excellent performance in cross-axis motion decoupling. The coupled motions on the center stage among different directions were experimentally determined to be $\leq 0.29 \mu\text{m}$. Repeatability testing demonstrates that the stage is capable of precise nanopositioning with an open-loop repeatability better than 17.3 nm along all three axes.

Acknowledgments

The authors thank the Natural Sciences and Engineering Research Council of Canada (NSERC) for funding and the Canadian Microelectronics Cooperation (CMC) for device fabrication support.

References

- [1] Toshiyoshi H, Su G J, LaCosse J and Wu M C 2003 A surface micromachined optical scanner array using photoresist lenses fabricated by athermal reflow process *J. Lightwave Technol.* **21** 1700–8
- [2] Kwon S and Lee L P 2002 Stacked two-dimensional micro-lens scanner for microconfocal imaging array *Proc. IEEE MEMS (Las Vegas, NV)* pp 483–6
- [3] Kim C H, Jeong H M, Jeon J U and Kim Y K 2003 Silicon micro XY -stage with a large area shuttle and no-etching holes for SPM-based data storage *J. Microelectromech. Syst.* **12** 470–8
- [4] Croft D and Devasia S 1999 Vibration compensation for high speed scanning tunneling microscopy *Rev. Sci. Instrum.* **70** 4600–5
- [5] Lee C W and Kim S W 1997 An ultraprecision stage for alignment of wafers in advanced microlithography *Precis. Eng.* **21** 113–22
- [6] Ku S S, Pinsopon U, Cetinkunt S and Nakajima S 2000 Design, fabrication, and real-time neural network control of a three-degrees-of-freedom nanopositioner *IEEE/ASME Trans. Mechatronics* **5** 273–80
- [7] Ru C H and Sun L N 2005 Improving positioning accuracy of piezoelectric actuators by feedforward hysteresis compensation based on a new mathematical model *Rev. Sci. Instrum.* **76** 095111
- [8] Shen S C, Pan C T and Chou H P 2002 Electromagnetic optical switch for optical network communication *J. Magn. Mater.* **239** 610–3
- [9] Xu Y, MacDonald N C and Miller S A 1995 Integrated micro-scanning tunneling microscope *Appl. Phys. Lett.* **67** 2305–7
- [10] Tuantranont A, Bright V M, Zhang J, Zhang W, Neff J A and Lee Y C 2001 Optical beam steering using MEMS-controllable microlens array *Sensors Actuators A* **91** 363–72
- [11] Bernstein J J, Taylor W P, Brazzle J D, Corcoran C J, Kirkos G, Odhner J E, Pareek A, Waelti M and Zai M 2004 Electromagnetically actuated mirror arrays for use in 3-D optical switching applications *J. Microelectromech. Syst.* **13** 526–35
- [12] Krishnamoorthy U, Lee D and Solgaard O 2003 Self-aligned vertical electrostatic combdrives for micromirror actuation *J. Microelectromech. Syst.* **12** 458–64
- [13] Miyajima H, Asaoka N, Isokawa T, Ogata M, Aoki Y, Imai M, Fujimori O, Katashiro M and Matsumoto K 2004 A MEMS electromagnetic optical scanner for a commercial confocal laser scanning microscope *J. Microelectromech. Syst.* **12** 243–51

- [14] Kim J and Lin L W 2005 Electrostatic scanning micromirrors using localized plastic deformation of silicon *J. Micromech. Microeng.* **15** 1777–85
- [15] Zhou L X, Kahn J M and Pister K S J 2006 Scanning micromirrors fabricated by a SOI/SOI wafer-bonding process *J. Microelectromech. Syst.* **15** 24–32
- [16] Joudrey K, Adams G G and McGruer N E 2006 Design, modeling, fabrication and testing of a high aspect ratio electrostatic torsional MEMS micromirror *J. Micromech. Microeng.* **16** 2147–56
- [17] Jaecklin V P, Linder C, De Rooij N F, Moret J M, Bischof R and Rudolf F 1992 Novel polysilicon comb actuators for *xy*-stages *Proc. IEEE MEMS Workshop (Travemunde, Germany)* pp 147–9
- [18] Kim C H and Kim Y K 2002 Micro *XY*-stage using silicon on a glass substrate *J. Micromech. Microeng.* **12** 103–7
- [19] Kwon H N, Lee J H, Takahashi K and Toshiyoshi H 2006 Micro *XY* stages with spider-leg acutators for two-dimensional optical scanning *Sensors Actuators A* **130–131** 468–77
- [20] Gu L, Li X X, Bao H F, Liu B, Wang Y L, Liu M, Yang Z X and Cheng B L 2006 Single-wafer-processed nano-positioning *XY*-stage with trench-sidewall micromachining technology *J. Micromech. Microeng.* **16** 1349–57
- [21] Lee C S B, Han S and MacDonald N C 2000 Single crystal silicon (SCS) *XY*-stage fabricated by DRIE and IR alignment *Proc. IEEE MEMS (Miyazaki, Japan)* pp 28–33
- [22] Bergna S, Gorman J J and Dagalakis N G 2005 Design and modeling of thermally actuated MEMS nanopositioner *Proc. ASME IMECE (Orlando, FL)* pp 1–8
- [23] Fan L, Wu M C, Choquette K D and Crawford M H 1997 Self-assembled microactuated *XYZ* stage for optical scanning and alignment *Proc. Int. Conf. Solid-State Sensors and Actuators (Chicago, IL)* pp 319–22
- [24] Ando Y 2004 Development of three-dimensional electrostatic stages for scanning probe microscope *Sensors Actuators A* **114** 285–91
- [25] Takahashi K, Mita M, Fujita H and Toshiyoshi H 2007 Topological layer switch technique for monolithically integrated electrostatic *XYZ*-stage *Proc. IEEE MEMS (Kobe, Japan)* pp 651–4
- [26] Gere J M 2004 *Mechanics of Materials* 6th edn (Boston: Brooks/Cole Thomson Learning)
- [27] Pan B, Xie H M, Xu B Q and Dai F L 2006 Performance of sub-pixel registration algorithms in digital image correlation *Meas. Sci. Technol.* **17** 1615–21
- [28] Sun Y, Piyabongkarn D, Sezen A, Nelson B J and Rajamani R 2002 A high-aspect-ratio two-axis electrostatic microactuator with extended travel range *Sensors Actuators A* **102** 49–60
- [29] Piyabongkarn D, Sun Y, Rajamani R, Sezen A and Nelson B J 2005 Travel range extension of MEMS electrostatic microactuators *IEEE Trans. Control Syst. Technol.* **13** 138–45